Optical Magnetic Multimodality Imaging of Plectin-1-Targeted Imaging Agent for the Precise Detection of Orthotopic Pancreatic Adenocarcinoma

Wenjia Zhang
Peking Union Medical College Hospital Department of Radiology
Xiaolong Liang
Peking University Third Hospital
Liang Zhu
Peking Union Medical College Hospital Department of Radiology
Xinyu Zhang
Peking Union Medical College Hospital Department of Radiology
Zhengyu Jin
Peking Union Medical College Hospital Department of Radiology
Yang Du
Chinese Academy of Sciences Institute of Automation
Jie Tian (jie.tian@ia.ac.cn)
CAS Key Laboratory of Molecular Imaging, Chinese Academy of Sciences https://orcid.org/0000-0003-0498-0432
Huadan Xue
Peking Union Medical College Hospital Department of Radiology

Research Article

Keywords: Pancreatic ductal adenocarcinoma (PDAC), magnetic particle imaging (MPI), superparamagnetic iron oxide nanoparticles (SPIONs), fluorescence molecular imaging (FMI), magnetic resonance imaging (MRI)

Posted Date: September 7th, 2021

DOI: https://doi.org/10.21203/rs.3.rs-865627/v1

Abstract

Purpose

Pancreatic ductal adenocarcinoma (PDAC) is a lethal malignancy worldwide. However, its early and precise detection is challenging currently. The novel magnetic particle imaging (MPI) is suitable for imaging tumours in deep organs because of its unlimited imaging depth, lack of background noise, and positive imaging signals. The purpose of this study was to utilize the MPI, in combination with fluorescence molecular imaging (FMI) and magnetic resonance imaging (MRI), to advance the precise detection of orthotopic PDAC xenografts *in vivo*.

Methods

The PDAC targeted Plectin-1 peptide and IRDye800CW was conjugated to the superparamagnetic iron oxide nanoparticles (SPIONs) (PTP-Fe_3O_4-IRDye800CW) for the PDAC targeted triple-modality imaging. Subcutaneous and orthotopic PDAC mouse models were established. FMI, MPI, and MRI were carried out for the dynamic and quantitative observation of PDAC tumours. Histological and immunohistochemical analyses were used as references for *ex vivo* validation.

Results

The probe showed good FMI, MPI, and MRI imaging performance *in vitro*. In *in vivo* subcutaneous and orthotopic PDAC xenograft models, the PTP-Fe_3O_4-IRDye800CW nanoparticles showed better PDAC targeted imaging with high specificity, uniform distribution, and longer retention effects for over 7 days compared with Con-Fe_3O_4-IRDye800CW nanoparticles.

Conclusion

Integration the imaging strengths of MPI, in combination with FMI and MRI could allow more precise detection of PDAC with high sensitivity and resolution. This may allow better diagnosis at molecular and cellular levels, potentially benefiting PDAC patients by providing early and sensitive detection. Moreover, this novel imaging methods may also provide guidance for the intraoperative detection and hyperthermia therapy for PDAC.

Introduction

Pancreatic cancer is one of the most fatal cancers globally and has a 5-year survival rate of 9% [1]. In clinical settings, few pancreatic ductal adenocarcinoma (PDAC) patients are diagnosed at early stages; meanwhile, more than 80% of patients are diagnosed in the advanced stages and miss the opportunity for surgery [2]. In addition, some PDAC patients with a late diagnosis show a poor response to chemotherapy [3]. Therefore, accurate imaging for aiding diagnosis and subsequent treatment is of great importance for improving the therapeutic efficacy and patient survival rate [4]. However, it is difficult to detect PDAC using current clinical imaging methods such as computed tomography (CT) and magnetic

resonance imaging (MRI), especially when it is located in the deep retroperitoneal space. As a consequence, there is an urgent requirement to identify new and promising imaging methods.

Molecular imaging is an emerging and indispensable tool for diagnosis and treatment of PDAC; it can detect diseases at the molecular and cellular levels [5–7]. Optical imaging techniques, for example, fluorescence molecular imaging (FMI), have the advantages of high sensitivity and free radiation; they can monitor the real-time pharmacokinetics and biodistribution of nanoparticles in the whole body but are limited by the low imaging depth due to light scattering [8]. MRI can provide morphological and anatomical details of deep tissues with excellent resolution and is widely used in clinics for PDAC diagnosis [9]. However, MRI has limited sensitivity and a negative signal when using superparamagnetic iron oxide nanoparticles (SPIONs) [10]. Moreover, over 30% of MRI depends on contrast agents such as gadolinium-based contrast agents, which show short blood lifetime, limited proton relaxation efficiency problem [11, 12].

Magnetic particle imaging (MPI) is a novel and developing imaging technique that was first utilized by Elaine et al. for cancer detection in 2017 [13, 14]. MPI is a novel tomographic imaging technique that detects SPION tracers with high contrast and sensitivity, linear quantitation and negligible tissue attenuation [13]. MPI is superior in its ability to directly detect the amount of SPIONs and provide positive signals instead of indirectly detecting them via hydrogen proton signal attenuation [15, 16]. MPI is also non-invasive and can quantitatively monitor the biodistribution of tracers that have no ionising radiation [14]. MPI shows some advantages over FMI and MRI, including deep imaging depth, which is especially suitable for orthotopic tumours; sensitive imaging, which is especially suitable for detecting small tumours; and ability to convert negative MRI signals into positive MPI signals. However, MPI shows no spatial information; hence, it can be combined with CT or MRI. Therefore, the combination of MPI with FMI and MRI not only utilizes their respective complementary advantages to carry out targeted tumour imaging, but also provides more accurate and deeper anatomical details for the precise imaging and detection of pancreatic ductal adenocarcinoma. To fulfil the above aim, the development of a corresponding triple FMI/MPI/MRI imaging agent is needed.

SPIONs are common imaging agents for MPI/MRI and provide an excellent nanoplatform for imaging various tumours[17, 18]. Some T2 contrast agents based on Fe_3O_4 nanoparticles have already been approved by the US Food and Drug Administration and have recently entered clinical trials [19]. Targeted SPIONs conjugated with specific ligands, including antibodies, peptides, and nucleotides, are considered ideal imaging probes with high biocompatibility and low toxicity [20–24]. Recent studies have shown that some biomarkers were successfully applied and improved the targeted and specific detection of PDAC in preclinical research, and Plectin-1 is a new and promising biomarker for pancreatic cancer. Kelly found that this targeted molecule was over-expressed in invasive pancreatic cancer [25]. Bausch demonstrated that 93% of PDAC cases were plectin-1 positive [26]. Furthermore, plectin-1 could distinguish malignant from benign cancer lesions with 84% sensitivity and 83% specificity. Plectin-1 is recognized as a biomarker of invasive and metastatic PDAC, and also a biomarker of pre-invasive pancreatic intraepithelial neoplasia (PanIN)-III lesions. Moreover, plectin-1 can distinguish PDAC from benign

inflammatory diseases for instance chronic pancreatitis; it was found in 100% of tested PDAC tumours and 60% of preinvasive PanIN-III lesions [26]. Therefore, plectin-1 may be a promising biomarker for specific and targeted PDAC imaging.

PDAC is characterised by hypovascular and hypoperfused tumour vessels and is usually surrounded by dense desmoplastic stroma [27]. A recent literature analysis demonstrated that only 0.4% of systemically administered nanoparticles were delivered to solid tumours in PDAC [28, 29], compared to an average median of 0.7 % in other cancer types [30]. Thus, it was concluded that the intensive permeability and retention effect (EPR) of nanoparticles did not work well in PDAC. In addition, as most SPIONs are delivered into the liver, spleen, and many other major organs, previous studies indicated that systemic SPION administration could give rise to iron overload [12]. Intratumoural injection could avoid this problem and has the potential for clinical translation for imaging-guided diagnosis and therapy, such as diagnosis by interventional endoscopic ultrasound and/or precise tumour excision [31].

In this study, we designed and synthesized plectin-1 peptide (PTP)-targeted and near-infrared dye IRDye800CW-conjugated SPIONs, abbreviated as PTP-Fe_3O_4-IRDye800CW, using Con-Fe_3O_4-IRDye800CW nanoparticles as a control. PTP-Fe_3O_4-IRDye800CW was applied to both the subcutaneous and orthotopic PDAC mouse models for FMI/MPI/MRI multimodality imaging (Fig. 1). We found that PTP-Fe_3O_4-IRDye800CW showed homogenous distribution and longer retention in PDAC compared to the non-targeted imaging probe Con-Fe_3O_4-IRDye800CW, which was restricted only to the injection site. In general, our targeted multimodality imaging probe showed more sensitive detection of PDAC with clear delineation of the tumour margin and exhibited good *in vivo* pharmacokinetic properties and safety. To our best knowledge, this is the first study to use novel MPI for *in vivo* pancreatic cancer imaging and complement it with FMI/MRI for a more comprehensive *in vivo* characterization of PDAC, allowing for more precise detection.

Materials And Experimental Methods

The details of the experimental materials and methods are available in the supporting information.

Results

Preparation and characterisation of PTP-Fe_3O_4-IRDye800CW nanoparticles

To ensure active targeting, DSPE-PEG-PTP and DSPE-PEG-CON were first synthesised by conjugating PTP to DSPE-PEG-NHS with an active carbonyl ester group via stable amide bonds, which was demonstrated using Fourier-transform infrared spectroscopy (FTIR) spectra (Supplementary Fig. 1a, 1b). And then, PTP-Fe_3O_4-IRDye800CW nanoparticles were generated by coating the surface of oleic acid-modified Fe_3O_4 with phospholipids of DSPE-PEG-PTP, DSPE-IRDye800CW, and DSPC. This process ensured that the resulting system could disperse well in aqueous solutions through the thin film hydration method, in which the mass ratio of oleic acid-modified Fe_3O_4 and phospholipids was 1:2. Meanwhile, the molar ratio

of DSPE-PEG-PTP and DSPE-IRDye800CW was 30:10:60. The thin film containing all these materials was hydrated with water and sonicated to obtain stable and dispersed nanoparticles. Transmission electron microscopy (TEM) observation demonstrated that the uniform size of PTP-Fe_3O_4-IRDye800CW nanoparticles was ~ 20 nm with square morphology (Fig. 2a), and dynamic light scattering revealed an average particle size of 27.2 nm (Supplementary Fig. 1c). The slightly larger size is likely due to the surface coating layer, which disrupts nanoparticle aggregation. The control group of Con-Fe_3O_4-IRDye800CW nanoparticles was prepared using the same procedure. The Con-Fe_3O_4-IRDye800CW was similar in size (~ 25.6 nm) and morphology (Fig. 2b, Supplementary Fig. 1d); thus, were well suited for subsequent comparison. The FTIR spectra of PTP-Fe_3O_4-IRDye800CW and Con-Fe_3O_4-IRDye800CW nanoparticles were further used to investigate the composition of the surface coating of Fe_3O_4. The spectra displayed characteristic peaks of DSPE-PEG-PTP or DSPE-PEG-CON and DSPE-IRDye800CW, which indicated successful modifications of the targeting group and fluorescent dye onto the nanoparticles (Fig. 2c, 2d).

The absorbance spectra of aqueous PTP-Fe_3O_4-IRDye800CW and Con-Fe_3O_4-IRDye800CW nanoparticles were further investigated. These spectra exhibited a wide and elevated absorption between and 550–850 nm and a maximum absorption at ~ 780 nm, which was slightly red-shifted compared to that of the free IRDye800CW. The highest peak was at 774 nm (Fig. 2e). This shift might be due to the interaction between IRDye800 CW and the cored Fe_3O_4. The IRDye800CW fluorescence emission spectra further indicated that both PTP-Fe_3O_4-IRDye800CW and Con-Fe_3O_4-IRDye800CW nanoparticles had similar fluorescence to free IRDye800CW upon light irradiation (the excitation and emission wavelengths were 740 nm and 795 nm, respectively) (Fig. 2f), confirming their ability to be used as fluorescent imaging probes for biological applications. Dispersed stability is an important way to mimic the *in vivo* environment. PTP-Fe_3O_4-IRDye800CW nanoparticles were well dispersed in various biological media without any precipitation, such as DMEM, FBS, RPMI-1640 cell medium, PBS, and deionised (DI) water (Supplementary Fig. 1e). These findings revealed that thes nanoparticles can be further utilized for the following imaging studies.

In vitro **FMI/MPI/MRI properties of PTP-Fe_3O_4-IRDye800CW nanoparticles**

The IRDye800CW on the PTP-Fe_3O_4-IRDye800CW nanoparticles can be utilized for FMI, and Fe_3O_4 can be utilized for MPI and T2-weighted MRI dual-modality imaging. To assess the FMI, MPI, and MRI T2 relaxivity properties of PTP-Fe_3O_4-IRDye800CW nanoparticles, we initially conducted FMI, MPI, and MRI measurements in the phantom. PTP-Fe_3O_4-IRDye800CW nanoparticles were prepared at different Fe concentrations, as identified by ICP-OES, to analyse the relevance of FMI, MPI, and MRI observations. The IRDye800CW fluorophore was conjugated to Fe_3O_4 at a ratio of 50:1. The fluorescence intensity was linearly correlated with the increased concentration of PTP-Fe_3O_4-IRDye800CW samples at Fe concentrations ranging from 0.3125–2.5000 μg/mL, as shown in Fig. 2g ($Y = 2.990 \times 10^8 X + 3.947 \times 10^7$, $R^2 = 0.998$, $P < 0.0001$). However, with the increase in sample concentration, the fluorescence intensity

tended to reach a plateau at 20.00 μg/mL due to the quenching effect. The MPI linear regression results and corresponding images are demonstrated in Fig. 2h, which shows that MPI signals increased with an increase in sample concentration ($Y = Y = 400.9 \times X + 18.38$, $R^2 = 0.9997$, $P < 0.0001$). Moreover, Fig. 2i shows the T2-weighted MRI of nanoparticles with reference to the sample concentration. The T2-weighted MR images of all the samples became dimming with incremental concentrations, indicating the samples as T2-negative contrast agents. The r1 of PTP-Fe_3O_4-IRDye800CW nanoparticles was calculated to be 44.4192 $mM^{-1}s^{-1}$ at 7.0 T.

Characterization of Plectin-1 expression in murine and human tumour PDAC xenografts

To validate plectin-1 as a specific molecular target for PDAC, the expression and location of human and murine pancreatic cell lines and tumour tissues were analysed. In BxPC3 human pancreatic tumour xenografts obtained from nude mice, high plectin-1 expression levels were detected by means of immunohistochemistry (Fig. 3a). Similarly, high expression of plectin-1 observed in pan02 murine pancreatic tumour xenografts from C57 mice (Fig. 3a). We found that plectin-1 was expressed at a high level in PDAC but not in other major organs, such as, the heart, liver, spleen, lung, and kidney (Fig. 3b). Flow cytometry data further quantified the cell surface and intracellular expression of plectin-1 in the pancreatic cancer cell lines. In Pan02 cells, 21.11% of the plectin-1 expression was observed on the cell surface, whereas 90.05% was observed in the cells. Similarly, 29.27% of the plectin-1 expression was observed on the BxPC3 cell surface, while 99.80% of the plectin-1 expression was observed intracellularly (Fig. 3c).

In vitro targeting specificity and cytotoxicity of PTP-Fe_3O_4-IRDye800CW nanoparticles

Cells were incubated with different concentrations of nanoparticles (2.5–80 μg/mL) for 24 h and their viability was examined. The data showed that no significant cytotoxicity was observed (Fig. 3d). Further, the binding specificity of PTP-Fe_3O_4-IRDye800CW nanoparticles for both murine (Pan02-Luc) and human (BxPC3-Luc) pancreatic cancer cells was assessed. Two pancreatic cancer cell lines were incubated with PTP-Fe_3O_4-fluorescein isothiocyanate (FITC) and Con-Fe_3O_4-FITC as the control, and laser scanning confocal microscopy was performed to examine their targeting ability. The pancreatic cancer cell uptake was obviously higher for PTP-Fe_3O_4-FITC nanoparticles than for Con-Fe_3O_4-FITC nanoparticles, which confirmed the specific pancreatic cancer cell targeting ability of the PTP peptide (Fig. 3e). The cytotoxicity assay was analyzed using the CCK-8 assay for both murine (Pan02-Luc) and human (BxPC3-Luc) pancreatic cancer cells. In general, the data showed that the PTP-Fe_3O_4-IRDye800CW nanoparticles possessed potential targeted imaging properties with good biocompatibility and biosafety.

In vivo MPI, FMI and MRI multimodality imaging for subcutaneous PDAC mouse model

MPI-FMI-MRI triple-modality imaging was initially performed on an *in vivo* subcutaneous mouse PDAC model. After intratumoural injection of PTP-Fe_3O_4-IRDye800CW or Con-Fe_3O_4-IRDye800CW nanoparticles, the FMI data demonstrated that PTP-Fe_3O_4-IRDye800CW had the highest fluorescence intensity at 4 h

post-injection and almost equal fluorescence intensity with Con-Fe_3O_4-IRDye800CW nanoparticles, and the fluorescence intensity decreased at 8 h post-injection. The FMI data demonstrated that PTP-Fe_3O_4-IRDye800CW also had a longer retention effect compared to the Con-Fe_3O_4-IRDye800CW nanoparticles (Fig. 4a). Quantitative analysis of the fluorescence intensity data was identical with the *in vivo* observations (Fig. 4b). The difference between the two sets of NFI (%) appeared 2 days post-injection (PTP-Fe_3O_4-IRDye800CW group: 43.68% ± 5.72% vs. Con-Fe_3O_4-IRDye800CW group: 31.79 ± 4.65%, $P < 0.05$), and we detected the NFI (%) until 7 days in the PTP-Fe_3O_4-IRDye800CW group (PTP-Fe_3O_4-IRDye800CW group: 30.41 ± 7.77% vs. Con-Fe_3O_4-IRDye800CW group: 13.13 ± 0.44%, $P < 0.05$). These results demonstrated that PTP-Fe_3O_4-IRDye800CW imaging nanoparticles showed better targeting and retention effects than Con-Fe_3O_4-IRDye800CW nanoparticles in the tumours.

Moreover, subcutaneous pancreatic tumour-bearing mice were simultaneously and dynamically monitored using MPI. MPI signal changes were observed for both PTP-Fe_3O_4-IRDye800CW and Con-Fe_3O_4-IRDye800CW nanoparticles at 4 h post-injection (Fig. 4c). Similarly, the MPI signals of the Con-Fe_3O_4-IRDye800CW nanoparticles were metabolised fast, and the PTP-Fe_3O_4-IRDye800CW group showed better targeted imaging at 2 d post-injection (PTP-Fe_3O_4-IRDye800CW group: 87.90 ± 5.55% vs. Con-Fe_3O_4-IRDye800CW group: 64.91 ± 6.97%, $P < 0.01$), whereas the PTP-Fe_3O_4-IRDye800CW group demonstrated homogeneous MPI signal distribution inside tumours and longer retention until 7 days (PTP-Fe_3O_4-IRDye800CW group: 72.66 ± 3.27% vs. Con-Fe_3O_4-IRDye800CW group: 49.95 ± 7.98%, $P < 0.05$). A quantitative analysis of MPI signals was further performed. The PTP-Fe_3O_4-IRDye800CW group retained 90.40% MPI signals, while the Con-Fe_3O_4-IRDye800CW group retained 64.91%. Moreover, the MPI signals decreased to half of that of the Con-Fe_3O_4-IRDye800CW group, but more than 72.66% of the MPI signal was observed in the PTP-Fe_3O_4-IRDye800CW group after a 7d metabolism (Fig. 4d).

As the representative clinical imaging modality, MPI was also performed. The results in Fig. 4e distinctly show that T2-weighted signals for the PTP-Fe3O4-IRDye800CW targeting probe in the coronal position gradually diffused through the whole PDAC xenografts, but the MRI signal was restricted to the injection site for the Con-Fe_3O_4-IRDye800CW group. Notably, the increased darker T2-weighted signals and prolonged retention caused by the PTP-Fe_3O_4-IRDye800CW targeting probe were retained for 7 d post-injection. In contrast, almost all the Con-Fe_3O_4-IRDye800CW probe stayed at the injection site for a short period of time and then was metabolised quickly. Compared with FMI, which provides only 2D information about the probe's metabolism, MRI offers more valuable and accurate anatomical details, which can locate the probe position within the tumour site.

To verify the *in vivo* triple-modality imaging observations, the tumours and major organs were obtained for further *ex vivo* multimodality imaging. As shown in Fig. 5a, *ex vivo* FMI images of the tumours and major organs from the mice injected with nanoparticles were obtained 2 days post-injection. Stronger fluorescence signals were observed in the resected tumours of the PTP-Fe_3O_4-IRDye800CW group than in the Con-Fe_3O_4-IRDye800CW group. No signals were detected in the liver, kidney, or spleen because the

probes were intratumourally injected. To further confirm that the MPI signal biodistribution, we performed *ex vivo* MPI scanning at 2 days post-injection. Tumours in the PTP-Fe_3O_4-IRDye800CW group had stronger MPI signals than those in the Con-Fe_3O_4-IRDye800CW group (Fig. 5b). Finally, histological and Prussian blue staining were performed, and the data demonstrated that more Fe-positive staining was evenly distributed inside the tumour in the PTP-Fe_3O_4-IRDye800CW group than in the Con-Fe_3O_4-IRDye800CW group (Fig. 5c). Furthermore, the liver and spleen tissues of the Con-Fe_3O_4-IRDye800CW group showed a small amount of Fe-positive staining in sporadic areas, but staining was barely detected in the PTP-Fe_3O_4-IRDye800CW group.

For the biosafety evaluation, we performed H&E staining of the major organs as well as liver and renal function. No abnormalities were found in major organs, such as the heart, liver, spleen, lung, and kidney (Supplementary Fig. 2a). In addition, ALT, AST, and ALP were tested for liver function. For renal function, serum creatinine (Scr) and blood urea nitrogen (BUN) levels were measured. The data showed that there were no differences between the two groups and the healthy normal mice group (Supplementary Fig. 2b).

In vivo **MPI, FMI and MRI multimodality imaging for orthotopic PDAC mouse model**

Based on our previous findings, we further performed targeted multimodality imaging of orthotopic PDAC xenografts, which can mimic the real tumour growth environment. The orthotopic mouse model was established using Pan02-Luc cells, and BLI was carried out to confirm the successful establishment of the orthotopic PDAC model (Supplementary Fig. 3a and 3b). The *in vivo* biodistribution and targeting specificity of the nanoparticles were investigated. The Pan02-Luc orthotopic PDAC tumour-bearing C57 mice were intratumourally injected with the imaging nanoparticles, and MPI-FMI-MRI triple-modality imaging was then carried out at different time points. As shown in Fig. 6a, FMI of both the PTP-Fe_3O_4-IRDye800CW and Con-Fe_3O_4-IRDye800CW groups showed the highest fluorescence signal at tumour sites at 4 h post-injection, which then reduced thereafter. The fluorescence signals in the PTP-Fe_3O_4-IRDye800CW group decreased more slowly compared to those in the Con-Fe_3O_4-IRDye800CW group. The difference in fluorescence intensity between two groups at the tumour site peaked at 2 d post-injection (PTP-Fe_3O_4-IRDye800CW group: 64.6 ± 7.03% vs. Con-Fe_3O_4-IRDye800CW group: 41.99 ± 0.12%, $P < 0.01$). Moreover, statistical difference of the fluorescence intensity between two groups could last for 7 d (PTP-Fe_3O_4-IRDye800CW group: 45.73 ± 6.42% vs. Con-Fe_3O_4-IRDye800CW group: 32.93 ± 0.76%, $P < 0.05$) (Fig. 6b). However, the problems associated with FMI of deep tumours are susceptible with light scattering and limited imaging depth etc [32]. Therefore, MPI is needed to overcome this problem.

MPI was further performed *in vivo*. As shown in Fig. 6c and 6d, the two groups displayed better MPI signals at 2 d post-injection (PTP-Fe_3O_4-IRDye800CW group: 85.72 ± 1.53% vs. Con-Fe_3O_4-IRDye800CW group: 74.41 ± 1.91%, $P < 0.01$), while the signals lasted up to 7 d post-injection in the PTP-Fe3O4-IRDye800CW group rather than Con-Fe3O4-IRDye800CW group (68.78 ± 7.75% vs. 49.66 ± 7.39%, $P < 0.05$). Moreover, 3D MPI/CT images showed a more intense and homogeneous distribution of the PTP-Fe_3O_4-IRDye800CW nanoparticles (Supplementary Video 1) compared to the Con-Fe_3O_4-IRDye800CW

nanoparticles (Supplementary Video 2) on the orthotopic PDAC tumours with details of the spatial positions of the whole body.

T2-weighted MRI was performed at the same time points. As shown in Fig. 6e, the PTP-Fe_3O_4-IRDye800CW nanoparticles were distributed throughout the tumour instead of being confined to the injection site as observed in the Con-Fe_3O_4-IRDye800CW group. Additionally, the PTP-Fe_3O_4-IRDye800CW nanoparticles were present for over 7 days, showing longer retention than the Con-Fe_3O_4-IRDye800CW nanoparticles. The MRI signals were consistent with the results of MPI and FMI. However, because of its intrinsic negative signals and susceptibility artifacts, MRI lacks the sensitivity to distinguish small or early-stage tumours and hypointense areas [33]. Consequently, it is necessary to achieve more comprehensive imaging information through multimodal imaging.

To further verify the *in vivo* multimodality imaging observations, we collected the pancreas with the tumours and major organs (spleen, liver, lung, heart, and kidney) of the mice at 2 d post-injection and examined their signal intensity. For *ex vivo* FMI, the fluorescence signals of tumours in the PTP-Fe_3O_4-IRDye800CW group were obviously stronger than those in the Con-Fe_3O_4-IRDye800CW group (Fig. 7a). In addition, the *ex vivo* MPI signals were further validated the tumours of PTP-Fe_3O_4-IRDye800CW group showed higher MPI signals than those of the Con-Fe_3O_4-IRDye800CW group, suggesting that the PTP-Fe_3O_4-IRDye800CW group showed longer signal retention than the Con-Fe_3O_4-IRDye800CW group (Fig. 7b). H&E and Prussian blue staining were further conducted, and the observations indicated that more Fe-positive staining was within the tumour in the PTP-Fe_3O_4-IRDye800CW group than the Con-Fe_3O_4-IRDye800CW group (Fig. 7c).

Discussion

Pancreatic cancer is the fourth leading cause of cancer-related mortality globally, with a 5-year survival rate of 9% [1]. To date, a series of molecular imaging studies of PDAC have been conducted. However, because the pancreas is located deep in the retroperitoneal space, many imaging methods are not suitable for the precise detection of PDAC. As each imaging modality has its own strengths and limitations, novel or multimodality molecular imaging is urgently needed for the precise detection of PDAC. In this study, PDAC targeted PTP-Fe_3O_4-IRDye800CW nanoparticles were developed as the targeted imaging probes for MPI, FMI and MRI triple-modality imaging of PDAC. As far as we know, this is the first time that MPI has been performed for the detection of the deep and positive detection signal of PDAC, and the complementation with FMI/MRI can provide sensitive and high spatial imaging signals. Multimodality imaging provides a potential strategy for the precise detection of orthotopic PDAC at the molecular level and can provide accurate guidance for PDAC therapy.

In vivo triple-modality imaging of both subcutaneous and orthotopic PDAC mouse models yielded consistent results. Through MPI and FMI, we concluded that the PTP-Fe_3O_4-IRDye800CW nanoparticles diffused more evenly inside the tumours than the Con-Fe_3O_4-IRDye800CW nanoparticles, thereby

facilitating the detection of the whole tumour with clear delineation of the tumour margin. PTP-Fe_3O_4-IRDye800CW nanoparticles also exhibited longer retention at tumour sites, which can effectively guide therapy. Notably, the MRI images confirmed that the PTP-Fe_3O_4-IRDye800CW nanoparticles penetrated more uniformly, evenly, and effectively than the Con-Fe_3O_4-IRDye800CW nanoparticles. This is mainly due to the driving force between the targeted binding of PTP peptide on the nanoparticles to the plectin-1 protein expressed on tumour cells. However, the Con-Fe_3O_4-IRDye800CW nanoparticles were limited to the injection site and did not spread to the dense tumour tissues. The inherently dark signal present in T2-weighted MRI often faces ambiguities from MRI artefacts, such as bleeding or calcification [34]. MPI, which shares the same SPIONs with MRI, can provide positive signals with no background interference [8]. Since the magnetization response of SPION is millions of times that of protons in water in MRI, MPI has a particularly high sensitivity (fe) (nanograms of Fe) [35]. Notably, MPI enabled the longitudinal tracking of nanoparticles in a living mouse model for 7 days.

Notably, we mainly utilized intratumoural injection for *in vivo* tumour imaging experiments. The advantages of this approach include that it can avoid lower nanoparticle infiltration to the PDAC tissues through tail vein injection due to the hypovascular properties of PDAC [27]. This method can also avoid excessive SPION accumulation in the liver and some major organs in the body, thereby avoiding unnecessary toxicity [12]. Moreover, the intratumoural injection method shows promise for clinical translation. Owing to the long-lasting accumulation of PTP-Fe_3O_4-IRDye800CW nanoparticles in pancreatic cancers, this method could assist in precise tumour excision and aid post-surgical or post-therapeutic follow-up imaging without further repetitive administration of contrast agents. For example, we could administer the probe during intraoperative laparoscopy for image guidance [31, 36]. Intratumoural injection also paves the way for subsequent therapy. First, we loaded the drug group to the nanoparticles so that the drug could be selectively delivered into the tumour by the targeted driving force [37]. Second, the SPIONs could be utilised as a magnetic hyperthermia platform, which may combine multimodal image-guided hyperthermia therapy [18].

In conclusion, the combination of MPI with FMI/MRI triple-modality imaging can facilitate precision and high-resolution detection of both subcutaneous and orthotopic PDAC *in vivo* at both the anatomical and molecular levels. Our triple-modality approach for PDAC imaging may have broad theranostic applications, such as sensitive tumour detection, delineation of tumour margin for intraoperative surgery, post-surgical follow-up imaging without repetitive administration of contrast agents, and guidance for targeted therapy such as magnetic hyperthermia therapy. Moreover, the main components of PTP-Fe_3O_4-IRDye800CW nanoparticles are relatively biocompatible materials, and hence, these nanoparticles possess potential for clinical translation and may be used for PDAC diagnosis and therapy in the future.

Declarations

Funding:

This article was funded by the National Natural Science Foundation of China (Grant number 82071896, 81871422, 81871514, 81227901, and 81771846), Beijing Natural Science Foundation under grant No. 7212207, the Elite Program of Dongcheng district of Beijing (Grant number 2020-dchrcpyzz-28), the Beijing Talents Foundation (2018000021223ZK48), and grants from Peking University Third Hospital (BYSYZD2019018, and jyzc2018-02), Ministry of Science and Technology of China under Grant No. 2017YFA0205200, 2017YFA0700401, the National Key Research and Development Program of China under Grant 2017YFA0700401.

Conflicts of interest:

The authors declare no conflicts of interests.

Availability of data and material:

The data used and/or analyzed during this study is available from the corresponding author on reasonable request.

Code availability:

Not applicable.

Author's contributions:

DY and XHD conceived the manuscript, ZWJ and LXL performed the experiments and wrote the manuscript; LZ, XYZ, YD, XHD, TJ, JZY revised the manuscript; XHD, TJ, JZY and DY supervised the manuscript.

Ethics approval:

All animal studies were performed according to the guidelines of the Institutional Animal Care and Use Committee at Peking University (Permit Number 2011-0039).

Consent to participate:

Not applicable.

Consent for publication:

Not applicable.

References

1. Siegel, R.L., K.D. Miller, and A. Jemal, *Cancer statistics, 2020.* CA Cancer J Clin, 2020. **70**(1): p. 7-30.
2. Willett, C.G., et al., *Locally advanced pancreatic cancer.* J Clin Oncol, 2005. **23**(20): p. 4538-44.

3. Zeng, S., et al., *Chemoresistance in Pancreatic Cancer.* Int J Mol Sci, 2019. **20**(18).
4. Eser, S., et al., *In vivo diagnosis of murine pancreatic intraepithelial neoplasia and early-stage pancreatic cancer by molecular imaging.* Proc Natl Acad Sci U S A, 2011. **108**(24): p. 9945-50.
5. Hu, Y., et al., *A Comparative Study of Clinical Intervention and Interventional Photothermal Therapy for Pancreatic Cancer.* Adv Mater, 2017. **29**(33).
6. Lee, G.Y., et al., *Theranostic nanoparticles with controlled release of gemcitabine for targeted therapy and MRI of pancreatic cancer.* ACS Nano, 2013. **7**(3): p. 2078-89.
7. Watabe, T., et al., *Theranostics Targeting Fibroblast Activation Protein in the Tumor Stroma: (64)Cu- and (225)Ac-Labeled FAPI-04 in Pancreatic Cancer Xenograft Mouse Models.* J Nucl Med, 2020. **61**(4): p. 563-569.
8. Song, G., et al., *A Magneto-Optical Nanoplatform for Multimodality Imaging of Tumors in Mice.* ACS Nano, 2019. **13**(7): p. 7750-7758.
9. Angelovski, G., *What We Can Really Do with Bioresponsive MRI Contrast Agents.* Angew Chem Int Ed Engl, 2016. **55**(25): p. 7038-46.
10. Zhu, L., et al., *Magnetic nanoparticles for precision oncology: theranostic magnetic iron oxide nanoparticles for image-guided and targeted cancer therapy.* Nanomedicine (Lond), 2017. **12**(1): p. 73-87.
11. Sherry, A.D. and M. Woods, *Chemical exchange saturation transfer contrast agents for magnetic resonance imaging.* Annu Rev Biomed Eng, 2008. **10**: p. 391-411.
12. Lazaro-Carrillo, A., et al., *Tailor-made PEG coated iron oxide nanoparticles as contrast agents for long lasting magnetic resonance molecular imaging of solid cancers.* Mater Sci Eng C Mater Biol Appl, 2020. **107**: p. 110262.
13. Gleich, B. and J. Weizenecker, *Tomographic imaging using the nonlinear response of magnetic particles.* Nature, 2005. **435**(7046): p. 1214-7.
14. Yu, E.Y., et al., *Magnetic Particle Imaging: A Novel in Vivo Imaging Platform for Cancer Detection.* Nano Lett, 2017. **17**(3): p. 1648-1654.
15. Wu, L., et al., *Organic Phase Syntheses of Magnetic Nanoparticles and Their Applications.* Chem Rev, 2016. **116**(18): p. 10473-512.
16. Goodwill, P.W., et al., *X-space MPI: magnetic nanoparticles for safe medical imaging.* Adv Mater, 2012. **24**(28): p. 3870-7.
17. Jiang, Z., et al., *Mixed Metal Metal-Organic Frameworks Derived Carbon Supporting ZnFe2O4/C for High-Performance Magnetic Particle Imaging.* Nano Lett, 2021. **21**(7): p. 2730-2737.
18. Du, Y., et al., *Optimization and Design of Magnetic Ferrite Nanoparticles with Uniform Tumor Distribution for Highly Sensitive MRI/MPI Performance and Improved Magnetic Hyperthermia Therapy.* Nano Lett, 2019. **19**(6): p. 3618-3626.
19. Bulte, J.W., *In vivo MRI cell tracking: clinical studies.* AJR Am J Roentgenol, 2009. **193**(2): p. 314-25.

20. Rosen, J.E., et al., *Iron oxide nanoparticles for targeted cancer imaging and diagnostics.* Nanomedicine, 2012. **8**(3): p. 275-90.
21. Briley-Saebo, K., et al., *Hepatic cellular distribution and degradation of iron oxide nanoparticles following single intravenous injection in rats: implications for magnetic resonance imaging.* Cell Tissue Res, 2004. **316**(3): p. 315-23.
22. Hsieh, W.J., et al., *In vivo tumor targeting and imaging with anti-vascular endothelial growth factor antibody-conjugated dextran-coated iron oxide nanoparticles.* Int J Nanomedicine, 2012. **7**: p. 2833-42.
23. Jie, L.Y., et al., *Actively-targeted LTVSPWY peptide-modified magnetic nanoparticles for tumor imaging.* Int J Nanomedicine, 2012. **7**: p. 3981-9.
24. Kumar, M., et al., *Cellular interaction of folic acid conjugated superparamagnetic iron oxide nanoparticles and its use as contrast agent for targeted magnetic imaging of tumor cells.* Int J Nanomedicine, 2012. **7**: p. 3503-16.
25. Kelly, K.A., et al., *Targeted nanoparticles for imaging incipient pancreatic ductal adenocarcinoma.* PLoS Med, 2008. **5**(4): p. e85.
26. Bausch, D., et al., *Plectin-1 as a novel biomarker for pancreatic cancer.* Clin Cancer Res, 2011. **17**(2): p. 302-9.
27. Adiseshaiah, P.P., et al., *Nanomedicine strategies to overcome the pathophysiological barriers of pancreatic cancer.* Nat Rev Clin Oncol, 2016. **13**(12): p. 750-765.
28. Dvorak, H.F., et al., *Identification and characterization of the blood vessels of solid tumors that are leaky to circulating macromolecules.* Am J Pathol, 1988. **133**(1): p. 95-109.
29. Dvorak, A.M., et al., *The vesiculo-vacuolar organelle (VVO): a distinct endothelial cell structure that provides a transcellular pathway for macromolecular extravasation.* J Leukoc Biol, 1996. **59**(1): p. 100-15.
30. Cheng, Y.H., et al., *Meta-Analysis of Nanoparticle Delivery to Tumors Using a Physiologically Based Pharmacokinetic Modeling and Simulation Approach.* ACS Nano, 2020. **14**(3): p. 3075-3095.
31. Oba, A., et al., *Staging laparoscopy for pancreatic cancer using intraoperative ultrasonography and fluorescence imaging: the SLING trial.* Br J Surg, 2021. **108**(2): p. 115-118.
32. Kwon, S. and E.M. Sevick-Muraca, *Effects of Depilation-Induced Skin Pigmentation and Diet-Induced Fluorescence on In Vivo Fluorescence Imaging.* Contrast Media Mol Imaging, 2017. **2017**: p. 7659242.
33. Kostura, L., et al., *Feridex labeling of mesenchymal stem cells inhibits chondrogenesis but not adipogenesis or osteogenesis.* NMR Biomed, 2004. **17**(7): p. 513-7.
34. Cai, X., et al., *Manganese Oxide Nanoparticles As MRI Contrast Agents In Tumor Multimodal Imaging And Therapy.* Int J Nanomedicine, 2019. **14**: p. 8321-8344.
35. Schenck, J.F., *The role of magnetic susceptibility in magnetic resonance imaging: MRI magnetic compatibility of the first and second kinds.* Med Phys, 1996. **23**(6): p. 815-50.

36. Newton, A.D., et al., *Intraoperative Near-infrared Imaging Can Identify Neoplasms and Aid in Real-time Margin Assessment During Pancreatic Resection.* Ann Surg, 2019. **270**(1): p. 12-20.
37. Gao, N., et al., *Tumor Penetrating Theranostic Nanoparticles for Enhancement of Targeted and Image-guided Drug Delivery into Peritoneal Tumors following Intraperitoneal Delivery.* Theranostics, 2017. **7**(6): p. 1689-1704.

Figures

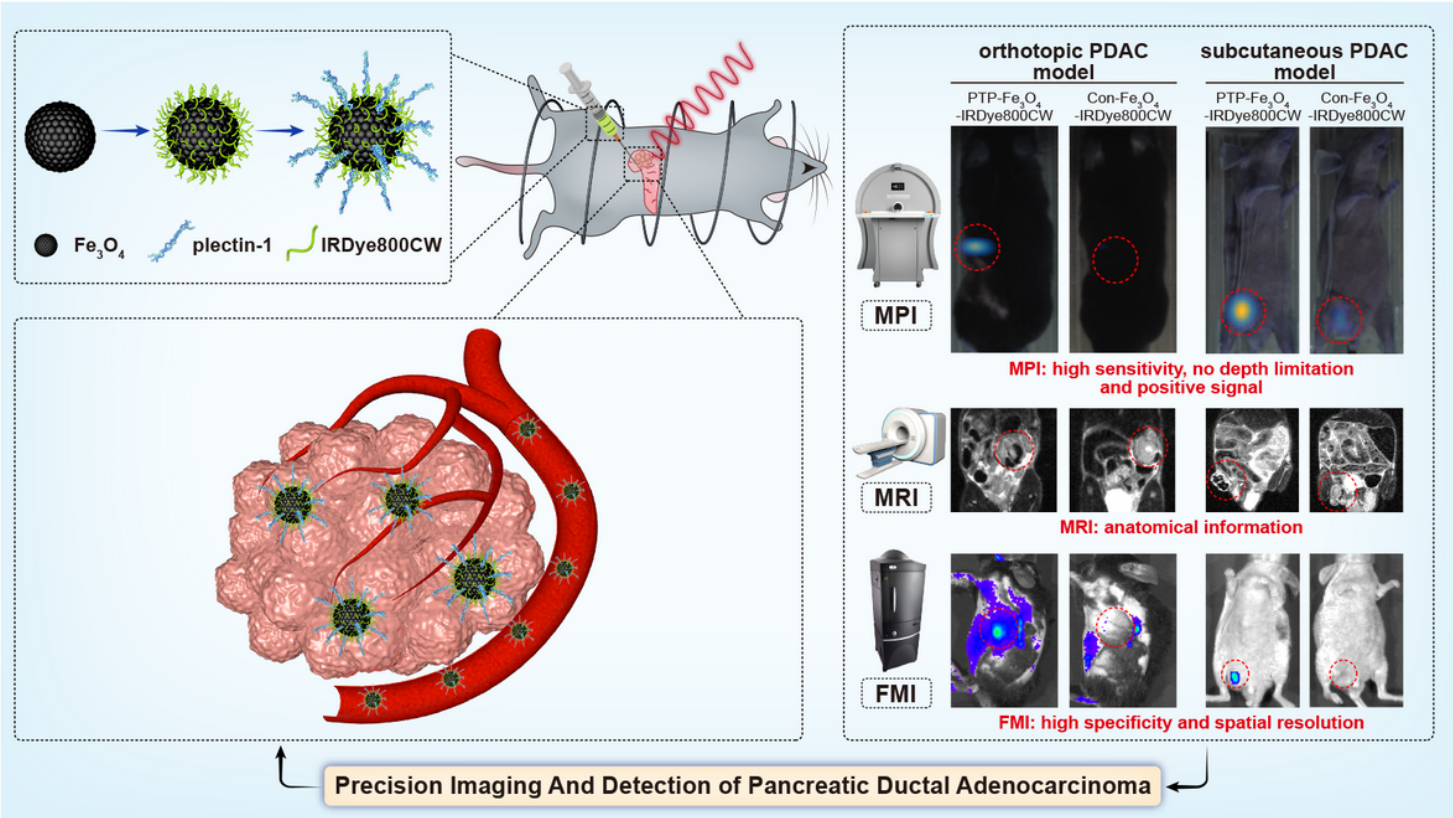

Figure 1

Schematic illustration of the multimodality imaging of orthotopic and subcutaneous pancreatic ductal adenocarcinoma (PDAC) using a targeted PTP-Fe3O4-IRDye800CW imaging agent. Multimodality imaging includes FMI, MPI and MRI.

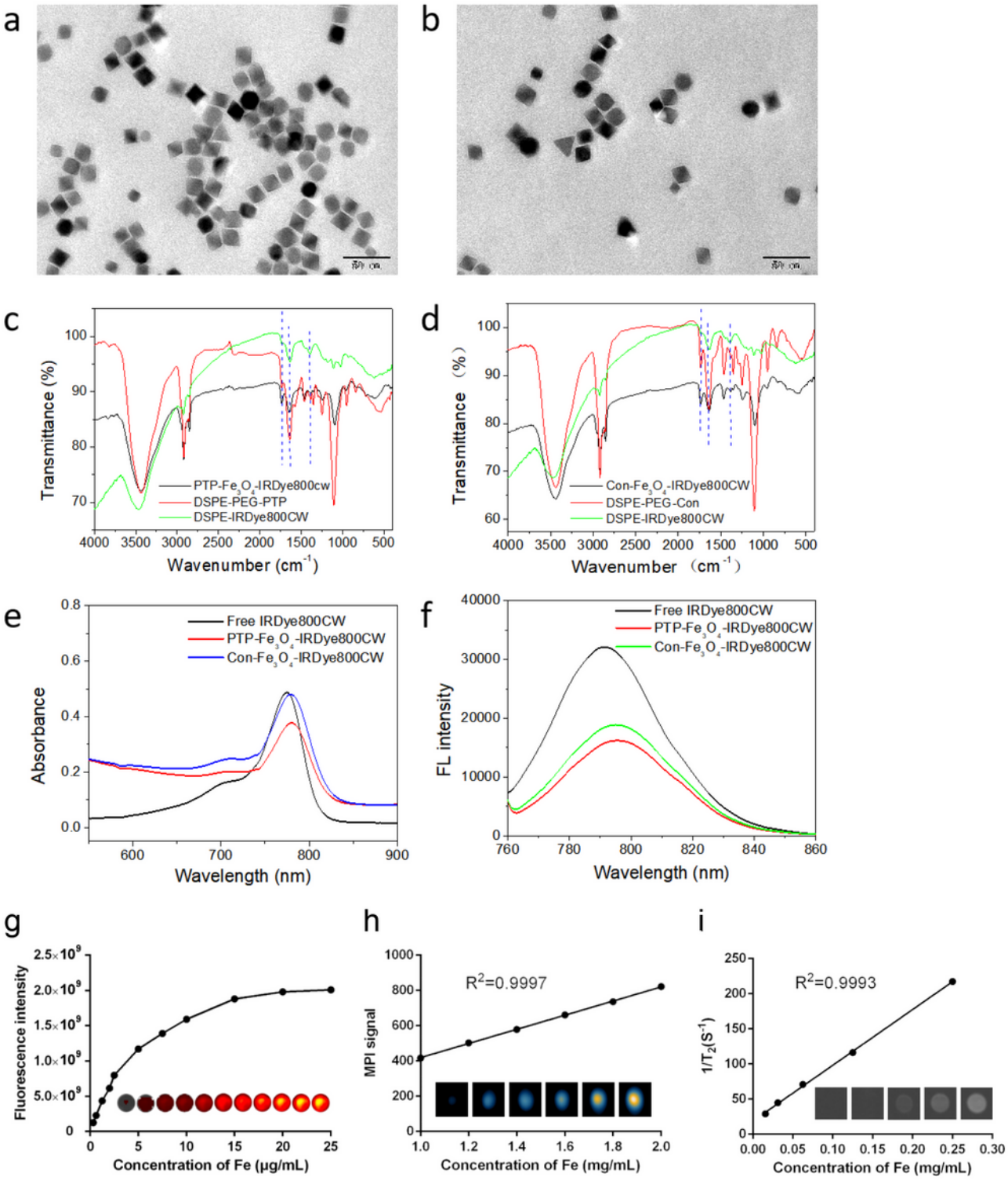

Figure 2

Characterisation of PTP-Fe3O4-IRDye800CW imaging agent. Transmission electron microscopy images of (a) PTP-Fe3O4-IRDye800CW and (b) Con-Fe3O4-IRDye800CW nanoparticles (scale bar: 50 nm). (c) Fourier-transform infrared spectrometry (FTIR) spectra of PTP-Fe3O4-IRDye800CW and (d) Con-Fe3O4-IRDye800CW nanoparticles. (e) Absorbance spectra and (f) fluorescence of PTP-Fe3O4-IRDye800CW nanoparticles. Con-Fe3O4-IRDye800CW and free IRDye800CW nanoparticles were used as controls. (g)

Fluorescence intensity of PTP-IRDye800CW nanoparticles increased with rising fluorophore concentrations using the IVIS spectrum. (h) Magnetic particle imaging (MPI) signals of PTP-Fe3O4-IRDye800CW nanoparticles increased with rising Fe concentrations. (i) Transverse (T2)-weighted MR images of PTP-Fe3O4-IRDye800CW nanoparticles at varying Fe concentrations.

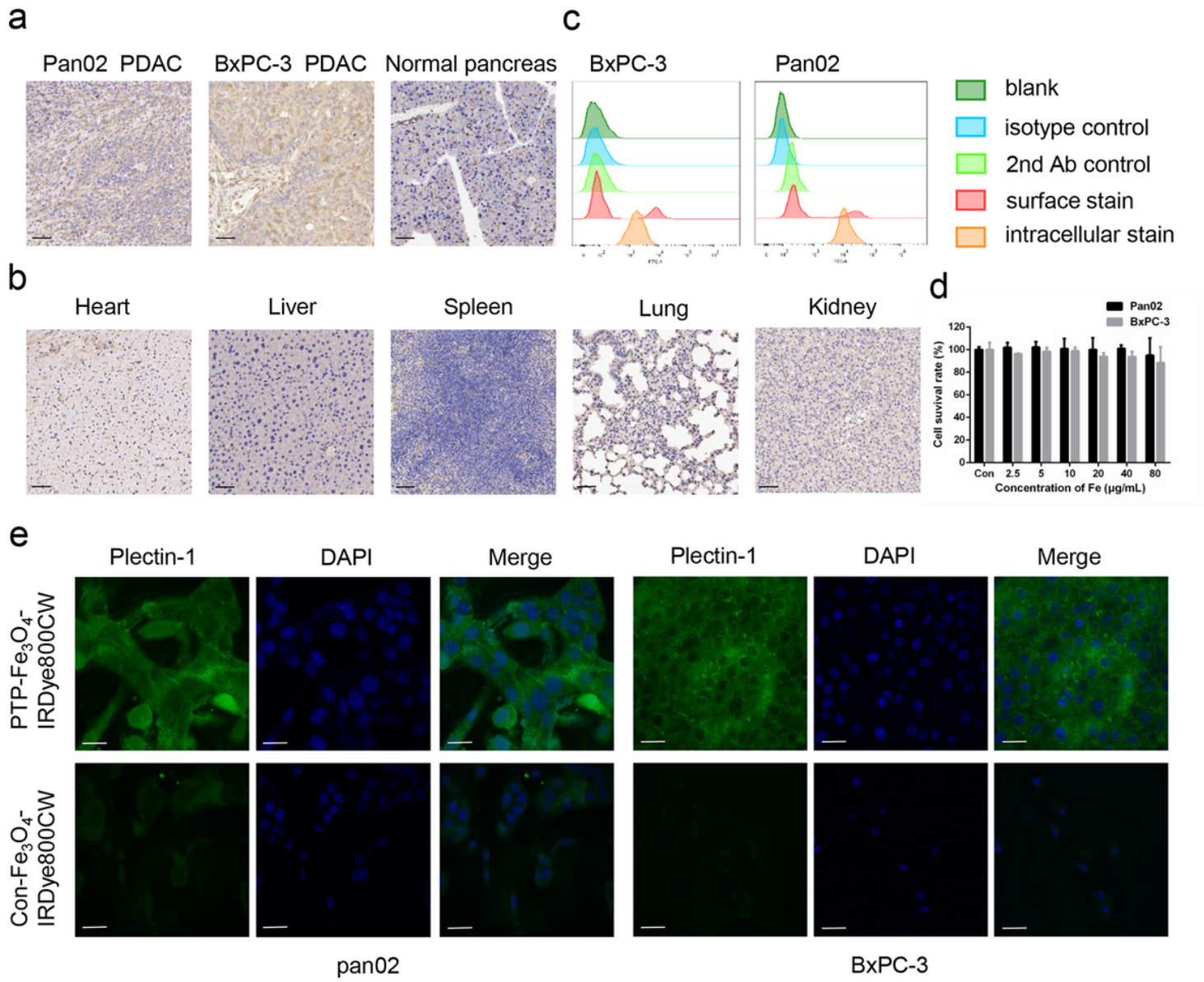

Figure 3

Examination of plectin-1 expression on pancreatic ductal adenocarcinoma (PDAC) and targeting specificity, and cytotoxicity of PTP-Fe3O4-IRDye800CW nanoparticles. (a) High levels of plectin-1 expression were detected by immunohistochemical staining in pancreatic tumour tissues from Pan02 and BxPC3 tumour-bearing mice but not on normal pancreatic tissues from healthy mice (scale bar: 50 μm). (b) Plectin-1 expression was not detected in the heart, liver, spleen, lung, or kidney (scale bar: 50 μm). (c) Plectin-1 expression in BxPC3 and Pan02 pancreatic cancer cell lines was determined by flow cytometry. (d) In vitro cytotoxicity of Pan02 and BxPC3 cells incubated with increasing concentrations of

PTP-Fe3O4-IRDye800CW nanoparticles. (e) Panc02 and BxPC3 cells were incubated with PTP-Fe3O4-FITC and Con-Fe3O4-FITC nanoparticles for 4 h for laser scanning confocal microscopy (scale bar: 25 μm).

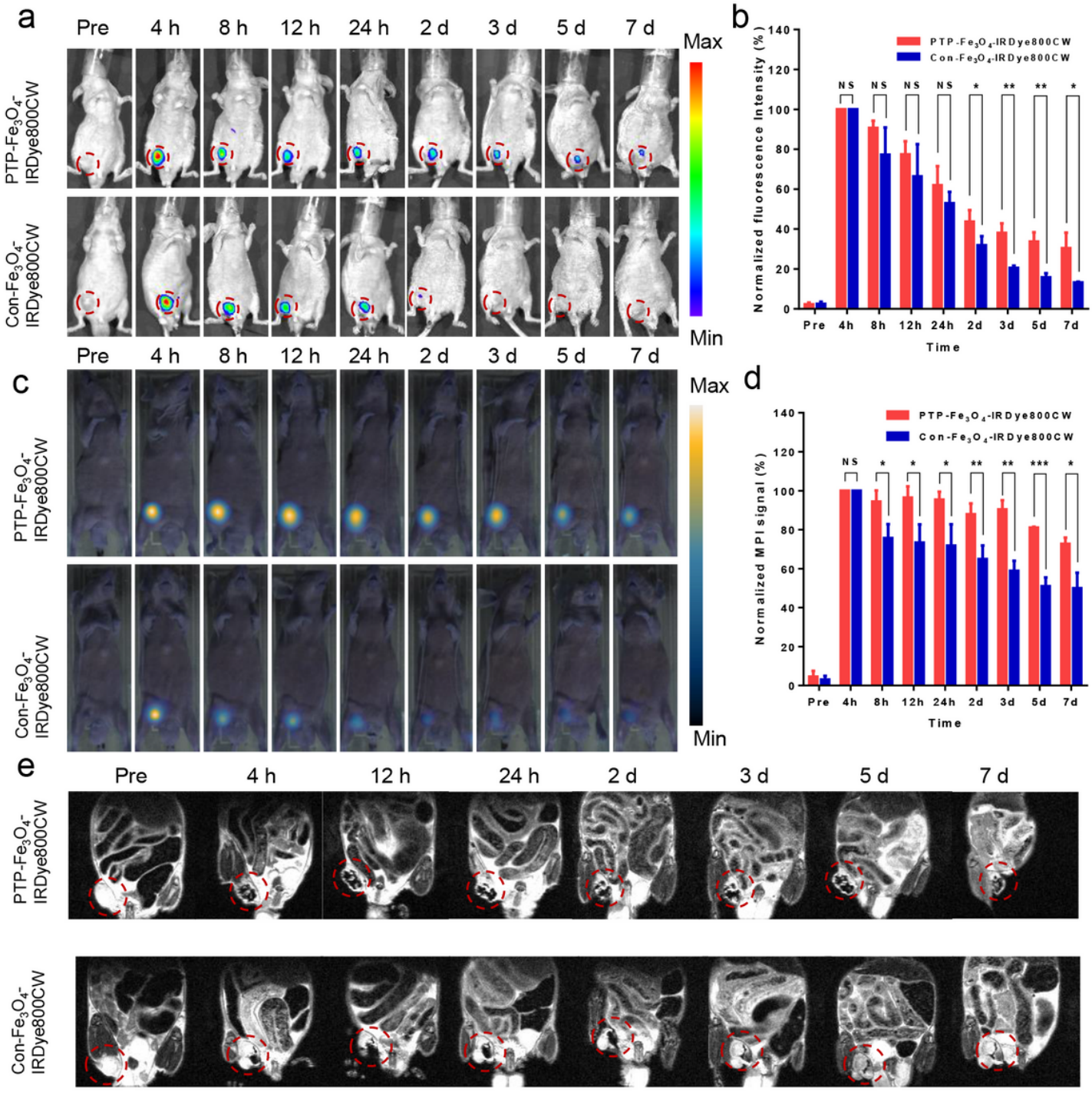

Figure 4

In vivo multimodality imaging of subcutaneous pancreatic ductal adenocarcinoma (PDAC) model. (a) Fluorescence images of subcutaneous mouse model in vivo at different time points. The red dotted circle represents the location of PDAC. (b) Quantitative comparison of normalised fluorescence intensity of the nanoparticles. (c) Magnetic particle imaging (MPI) images of subcutaneous PDAC mouse model in vivo

at different time points. (d) Quantitative comparison of normalised MPI signal of the nanoparticles. (e) MRI images of subcutaneous mouse model in vivo at different time points. *, P < 0.05; **, P < 0.01; ***, P < 0.001

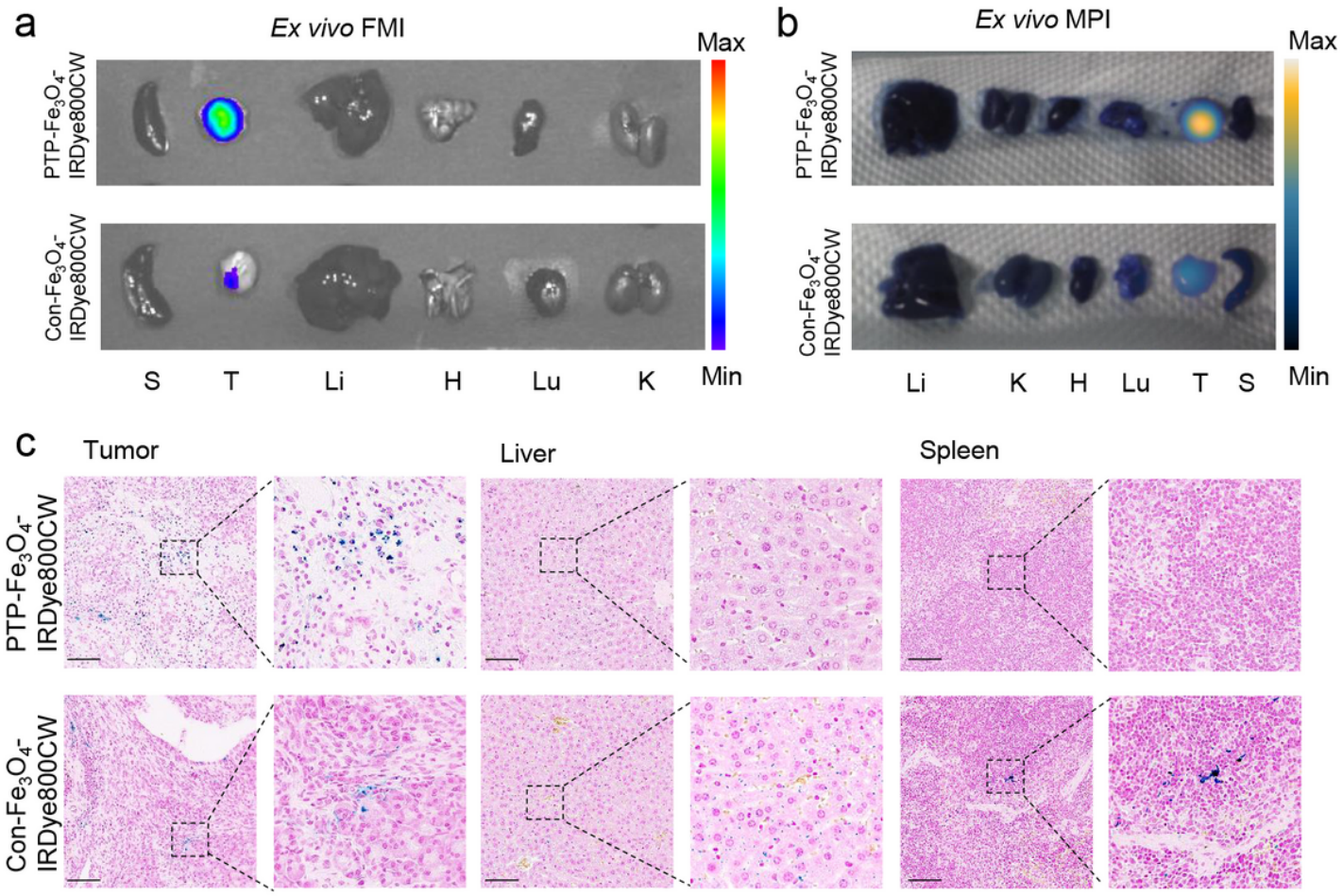

Figure 5

Ex vivo imaging of subcutaneous pancreatic ductal adenocarcinoma (PDAC) model and Prussian blue staining. Ex vivo fluorescence images (a) and magnetic particle imaging (MPI) images (b) of resected tumours and major organs from the subcutaneous model 2 d after injection. S: spleen. T: tumour. Li: liver. H: heart. Lu: lung. K: kidney. (c) Prussian blue staining of resected subcutaneous tumours, liver, and spleen (scale bar: 50 μm)

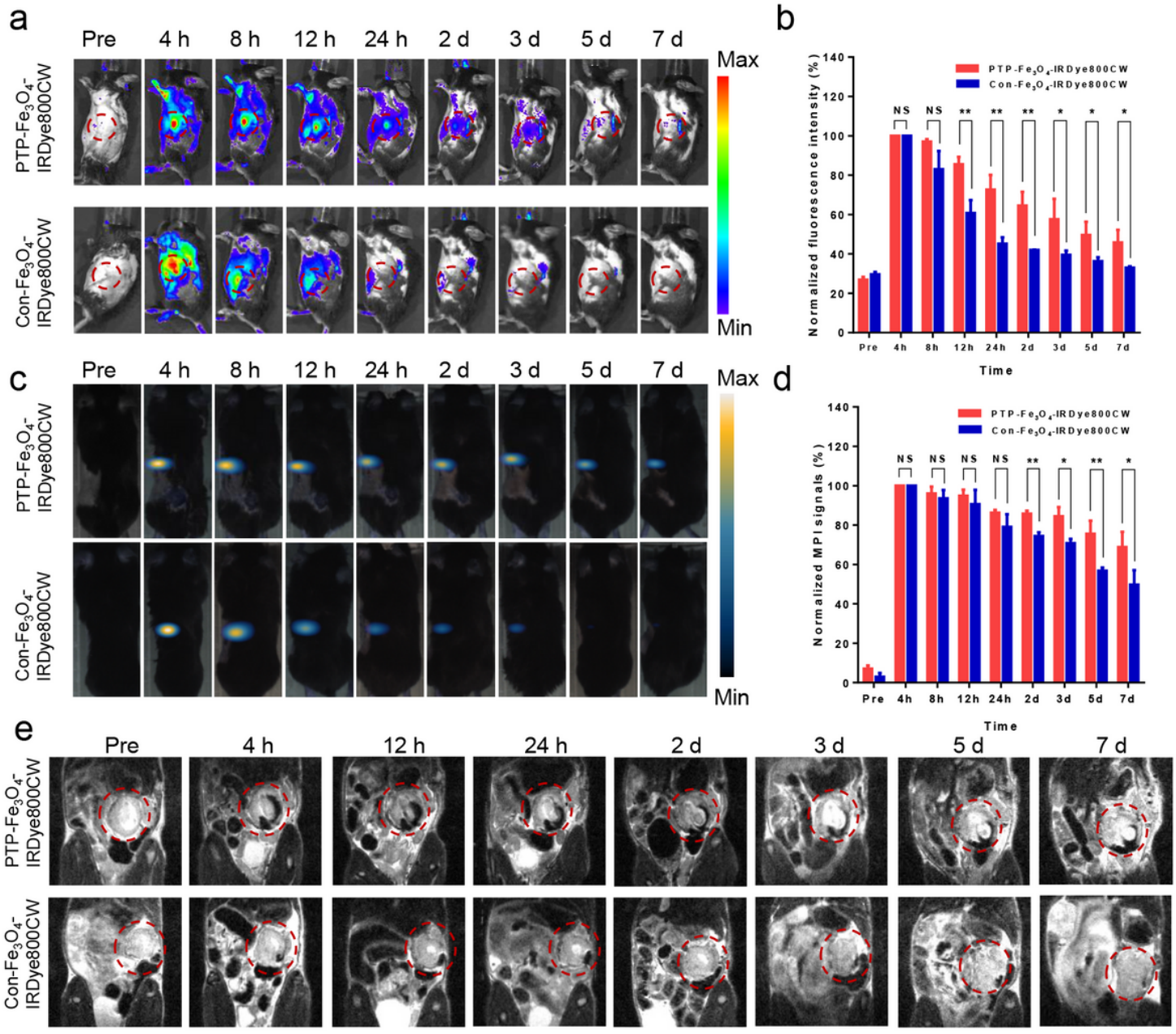

Figure 6

In vivo multimodality imaging of orthotopic pancreatic ductal adenocarcinoma (PDAC) model. (a) Fluorescence images of orthotopic mouse model in vivo at different time points. The red dotted circle represents the location of PDAC in situ. (b) Quantitative comparison of normalised fluorescence intensity of the nanoparticles. (c) Magnetic particle imaging (MPI) images of orthotopic mouse model in vivo at different time points. (d) Quantitative comparison of normalised MPI signal of the nanoparticles. (e) MRI images of orthotopic mouse model in vivo at different time points. *, P < 0.05; **, P < 0.01; ***, P < 0.001

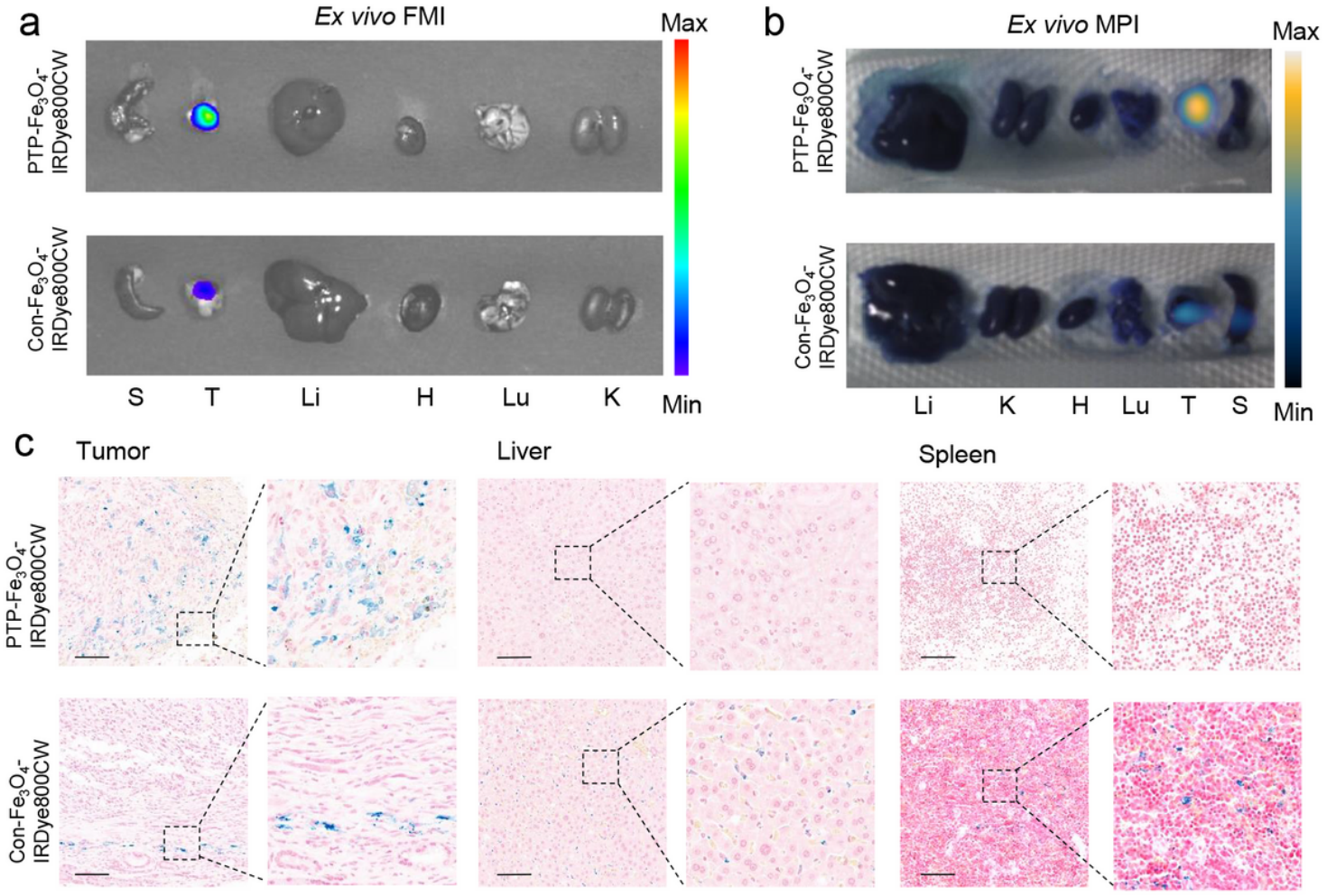

Figure 7

Ex vivo imaging of orthotopic pancreatic ductal adenocarcinoma (PDAC) model and Prussian blue staining. Ex vivo fluorescence images (a) and magnetic particle imaging (MPI) images (n) of resected PDAC tumours and major organs from the orthotopic model 2 d after injection. S: spleen. T: tumour. Li: liver. H: heart. Lu: lung. K: kidney. (c) Prussian blue staining of resected orthotopic tumours, liver, and spleen (scale bar: 50 μm)

Supplementary Files

This is a list of supplementary files associated with this preprint. Click to download.

- Supplementaryvideo1.mp4
- Supplementaryvideo2.mp4
- supplementarymaterials.doc